Volume 3
Number 23
7 December 2021
Pages 6505–6752

Nanoscale Advances

rsc.li/nanoscale-advances

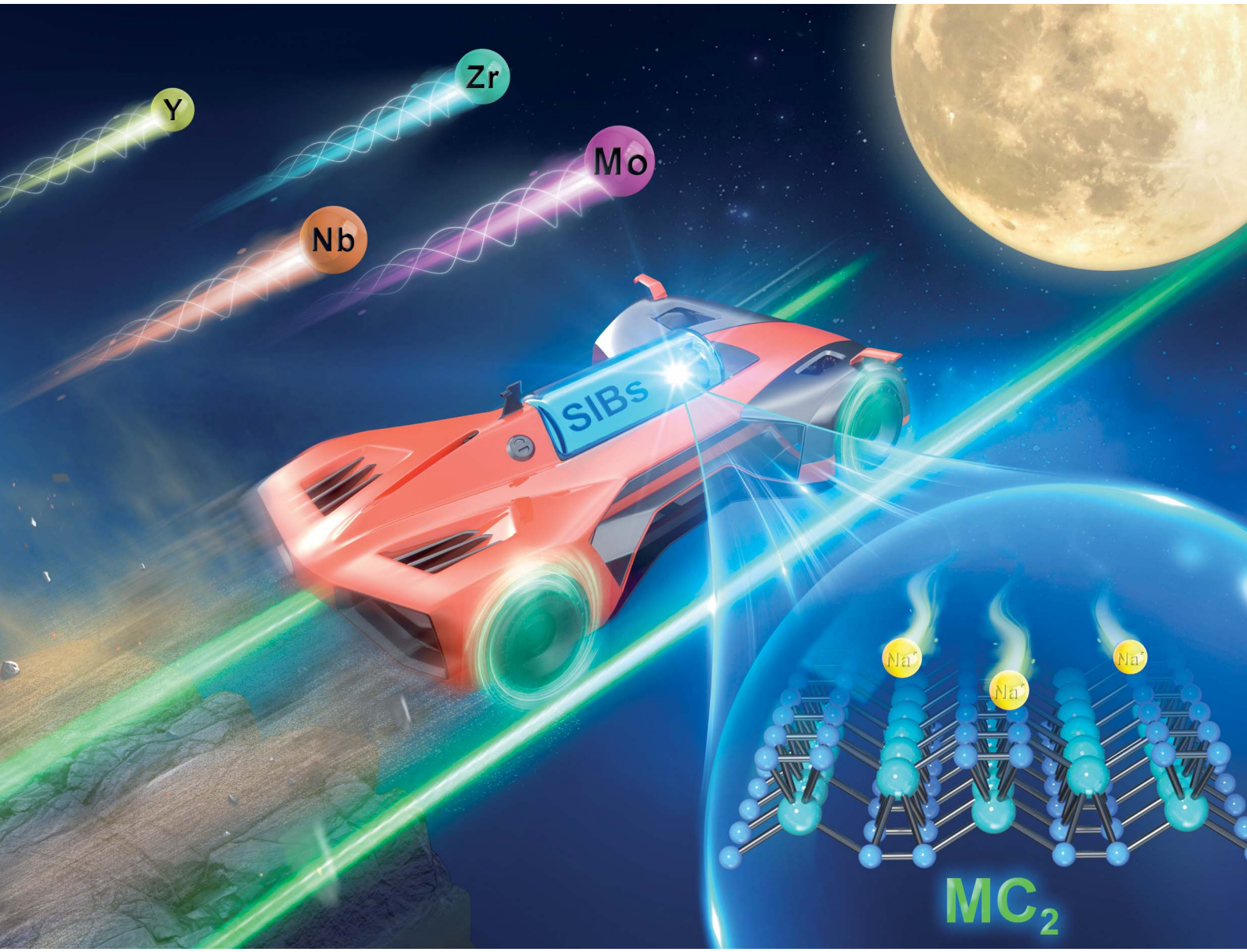

ISSN 2516-0230

ROYAL SOCIETY OF CHEMISTRY

PAPER

Xiaodong Lv, Fengyu Li *et al.*

MC_2 (M = Y, Zr, Nb, and Mo) monolayers containing C_2 dimers: prediction of anode materials for high-performance sodium ion batteries

NCNST

Nanoscale Advances

ROYAL SOCIETY OF CHEMISTRY

PAPER

View Article Online
View Journal | View Issue

Cite this: *Nanoscale Adv.*, 2021, **3**, 6617

MC_2 (M = Y, Zr, Nb, and Mo) monolayers containing C_2 dimers: prediction of anode materials for high-performance sodium ion batteries†

Zhanzhe Xu,[a] Xiaodong Lv,*[bcd] Wenyue Gu[a] and Fengyu Li *[a]

Seeking novel high performance anode materials for sodium ion batteries (SIBs) is an attractive theme in developing energy storage devices. In this work, by means of density functional theory computations, we predicted a family of MC_2 (M = Y, Zr, Nb, and Mo) monolayers containing C_2 dimers to be promising anode materials for SIBs. The stability, electronic structure, and adsorption/diffusion/storage behavior of sodium atoms in MC_2 (M = Y, Zr, Nb, and Mo) monolayers were explored. Our computations revealed that Na adsorbed MC_2 (M = Y, Zr, Nb, and Mo) monolayers show metallic characteristics that give rise to excellent electrical conductivity and Na mobility with low activation energies for diffusion (0.21, 0.04, 0.20, and 0.22 eV, respectively) in these materials, indicative of a high charge/discharge rate. In addition, the theoretical capacities of Na-adsorbed on YC_2, ZrC_2, NbC_2, and MoC_2 monolayers are 478, 697, 687, and 675 mA h g^{-1}, respectively, higher than that of commercial graphite (284 mA h g^{-1}), and the open-circuit voltages are moderate (0.11–0.25 V). Our results suggest that MC_2 (M = Y, Zr, Nb, and Mo) monolayers have great potential to serve as anode materials for SIBs.

Received 4th June 2021
Accepted 17th September 2021

DOI: 10.1039/d1na00422k

rsc.li/nanoscale-advances

1. Introduction

The global demand for advanced energy storage and conversion technologies, especially electrochemical energy technologies, is growing rapidly. Among them, rechargeable batteries, such as lithium-ion batteries (LIBs), are widely used in mobile electronic and electrified vehicles.[1–3] However, LIBs can meet the tough demands of energy storage and conversion applications, yet the limited abundance (only 20 ppm) and expensiveness of lithium are not the best choices for application in large-scale energy storage systems and sustainability.[4,5] Fortunately, sodium-ion batteries (SIBs) were confirmed as low-cost alternatives to lithium-ion batteries (LIBs) in energy storage applications, on account of the natural abundance, high energy density and similar intercalation chemistry to lithium, suggesting that some mature technologies in LIBs can be translated to SIBs, and SIBs are promising candidates for next generation rechargeable batteries.[6]

Cathode materials with high electrochemical performance for SIBs have been extensively studied experimentally and theoretically, such as layered transition metal oxide compounds, polyanionic compounds, Prussian blue analogues, and sodium-based layered materials.[7,8] However, anode materials matching well LIB systems are not suitable for SIBs due to the bigger ionic radius and the higher redox potential of Na^+ ions *vs.* Li^+. For instance, graphite is not available in SIBs, because the interlayer distance of graphite is too small to accommodate sodium, leading to a larger mismatched layer spacing and poor capacity.[9,10] Thus, the design and exploration of suitable electrode materials for SIBs are greatly desired.

In recent years, two-dimensional (2D) materials as electrodes have attracted great attention due to their excellent properties, including good mechanical flexibleness, rich active sites, large exposed surface area for electrochemical processes, and expanded interlayer spacing.[11,12] For example, transition metal chalcogenides (TMDs),[13–15] oxides (TMOs),[16,17] borides (MBenes),[18,19] transition metal carbides or nitrides

[a]*School of Physical Science and Technology, Inner Mongolia University, Hohhot, 010021, China. E-mail: fengyuli@imu.edu.cn*

[b]*CAS Key Laboratory of Magnetic Materials and Devices, Ningbo Institute of Materials Technology and Engineering, Chinese Academy of Sciences, Ningbo 315201, China. E-mail: lvxiaodong@nimte.ac.cn*

[c]*Zhejiang Province Key Laboratory of Magnetic Materials and Application Technology, Ningbo Institute of Materials Technology and Engineering, Chinese Academy of Sciences, Ningbo 315201, China*

[d]*Ganjiang Innovation Academy, Chinese Academy of Sciences, Ganzhou 341000, People's Republic of China*

† Electronic supplementary information (ESI) available: Lattice constants of the MC_2 monolayers; bond length and thickness of the MC_2 monolayers; the calculated phonon spectra of the MC_2 monolayers; the FPMD simulations at the end of 5 ps at 300 K; the electronic localization function (ELF) of the MC_2 monolayers; the partial density of states (TDOS and PDOS) of the MC_2 monolayers; the partial density of states (PDOS) of Na-adsorbed MC_2 monolayers; the variation of the path-I diffusion lengths of Na on the MC_2 monolayers with the lattice constants of MC_2; the energy profile (left plane) and diffusion pathways (right plane) of Na diffusing on the TiC_2 monolayer; the formation energy (E_f) of Na_xMC_2 with respect to MC_2 monolayers and Na bulk bcc metal; the configurations and their optimized adsorption energies (eV) for Na_xNbC_2; the side views of the Na-intercalated MC_2 monolayer at the end of 5 ps FPMD simulations at 300 and 500 K, respectively. See DOI: 10.1039/d1na00422k

(MXenes),[20,21] and main group binary compounds (B_2S, BN_2, SiS, SnP_3, *etc.*)[22–25] have been theoretically and experimentally explored as anode materials. Among these materials, 2D MXenes have experienced rapid development as anode materials after the successful exfoliation of Ti_3C_2 nanosheets in 2011,[26] due to their superior electrical conductivity, high performance rate, and high specific capacities.[27–30] So far, metal-rich 2D MXene-based materials (*i.e.* Ti_2C,[31] V_2C,[32] Nb_2C,[33] Mo_2C,[34] Cr_2C,[35] Mn_2C,[36] *etc.*) have been extensively studied as anode materials for LIBs and SIBs. However, the major problems with MXenes are surface functionalization and metal atoms exposed on the surface commonly to suppress sodium adsorption, which largely reduce the storage capacity and the performance of batteries.[21]

In this regard, Wang *et al.*[37] proposed a novel carbon-rich 2D metal carbide (MC), namely TiC_2 monolayer, which consists of unique C_2 dimers (Fig. 1a) and exhibits high structural stability. The Li capacity, open-circuit voltage (OCV), and diffusion barrier were calculated to be 622 mA h g^{-1}, 0.96 V, and 0.11 eV, respectively, indicating that the TiC_2 monolayer is a promising anode material for LIBs. Subsequently, other transition metal carbide (VC_2,[38,39] TaC_2,[40] MnC_2,[41] ScC_2,[42] and WC_2 (ref. 43)) monolayers with a similar configuration were also theoretically investigated as LIB and SIB anode materials. In particular, Zhao *et al.*[44] found that an FeC_2 monolayer containing isolated C_2 dimers with ferromagnetic and half-metallic properties was possible to be synthesized by chemically exfoliating the bulk counterpart of $ThFeC_2$.

Therefore, the proposal of C-rich MC_2 monolayers may offer a new strategy for the rational design of 2D anode materials for SIBs. In this work, four C_2-containing MC_2 (M = Y, Zr, Nb and Mo) monolayers were systematically explored by means of DFT computations. According to our calculations of cohesive energy, phonon dispersion, first-principles molecular dynamics (FPMD) stimulation, mechanical parameters, and sodium adsorption/diffusion/capacity, the four examined monolayers were confirmed to exhibit great thermodynamic, dynamic, thermal, and mechanical stability, excellent electronic conductivity and outstanding electrode performance as a SIB anode material. In particular, the ZrC_2 monolayer exhibits superior electrochemical performance with high theoretical storage capacity (699 mA h g^{-1}) and small diffusion energy barriers (0.04 eV) for Na atoms.

2. Computational methods

In this study, the structural relaxation and performance calculations were based on density functional theory (DFT) methods within the Vienna *ab initio* simulation package (VASP).[45–47] The general gradient approximation (GGA) in the form of Perdew–Burke–Ernzerhof (PBE) exchange and correlation functional and a plane wave basis set with an energy cut-off of 500 eV were employed.[48,49] Monkhorst–Pack meshes[50] of 11 × 11 × 1 and 5 × 5 × 1 *k*-points were used to sample the two-dimensional Brillouin zone for the unit cell and supercell relaxation and electronic structure calculations, respectively. An inter-layer vacuum space of 20 Å was used to avoid the interactions of mirror images in adjacent layers. All the structures are fully relaxed until the convergence tolerances for the energy and force on each atom were less than 1.0×10^{-5} eV and 0.02 eV $Å^{-1}$, respectively. All the atomic structures and charge density distributions were visualized by using the VESTA package.[51]

The dynamic stability of MC_2 (M = Y, Zr, Nb, and Mo) monolayers was evaluated by recording the phonon spectrum with the PHONOPY code[52] on the basis of density functional perturbation theory (DFPT). Thermal stabilities were assessed by performing first-principles molecular dynamics (FPMD) simulations (a 4 × 4 × 1 supercell, 96 atoms) in the NVT ensemble lasting for 5 ps with a time step of 1 fs at room temperature (300 K), and the temperature was controlled by the Nosé–Hoover method.[53] By using the climbing-image nudged elastic band (CI-NEB) approach,[54,55] the diffusion energy barrier

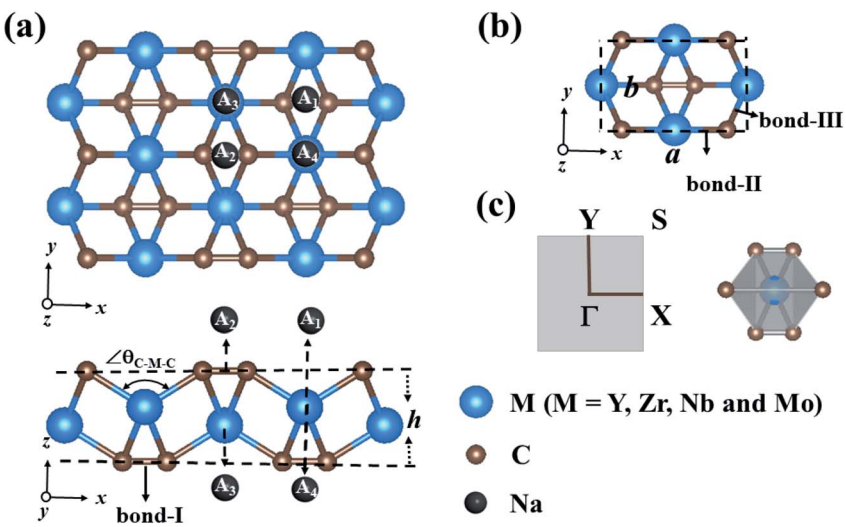

Fig. 1 (a) The geometric structure of the 2 × 2 × 1 supercell of the MC_2 (M = Y, Zr, Nb, and Mo) monolayers (top and side views); (b) the unit cell is highlighted by the black dashed lines; (c) the Brillouin zone of the MC_2 monolayers and the edge-shared MC_6 octahedral structure.

and the minimum energy pathways of Na atom diffusing on MC_2 (M = Y, Zr, Nb, and Mo) monolayers were calculated. The charge distribution and transfer were analyzed by the Bader charge method.[56]

3. Results and discussion

3.1 Geometric structure of the MC_2 (M = Y, Zr, Nb, and Mo) monolayers

The optimized structures of MC_2 (M = Y, Zr, Nb, and Mo) monolayers are displayed in Fig. 1a. From the top view, these monolayers exhibit a rectangular lattice with the space group *Pmmn* symmetry, where carbon atoms are in the form of C_2 dimers, and each unit cell contains two M atoms and four C atoms (Fig. 1b). From the side view, the crystal structure of the MC_2 (M = Y, Zr, Nb, and Mo) monolayers possesses a tetra-layer structure with two M layers sandwiched between two C layers, in which each M atom bonds with six neighboring C atoms, while each C atom is shared by one C of the same C_2 dimer and three adjacent M atoms, forming an edge-shared MC_6 octahedral structure without M atoms exposed on the surface (Fig. 1c).

Table 1 summarizes the optimized structural parameters of MC_2 (M = Y, Zr, Nb, and Mo) monolayers, including the lattice constants (a and b), bond lengths of C–C (bond I), M–C (bond II along the x axis and bond-III along the y axis) and thickness (h), and the evolution trend was plotted for different MC_2 monolayers with transition metal atoms (M) from Y → Mo (Fig. S1 and S2†). The lattice constants ($4.84 \leq a \leq 5.80$ Å and $3.01 \leq b \leq 4.28$ Å) are close to those of VC_2 ($a = 4.62$ Å and $b = 3.28$ Å),[38] FeC_2 (4.54 Å and 2.89 Å),[44] and ScC_2 (5.39 Å and 4.12 Å).[42] The remarkable feature we can see is that structural parameters, such as lattice constants (a and b), bond lengths M–C (d_{M-C}) and bond angle ($\angle\theta_{C-M-C}$), decrease from 5.77 to 4.84 Å (4.45 to 3.03 Å), 2.39 to 2.03 Å (2.51 to 2.26 Å) along the x (y)-direction and 138.14° to 119.28° from Y → Mo (Fig. S3†), mainly originating from the decrease of the atomic radius from Y to Mo. However the others, including bond lengths C–C (d_{C-C}) and thickness (h), increase (1.30 to 1.37 Å and 1.81 to 2.60 Å) from Y → Mo, respectively. The latter increasing trend could be understood by the electronegativity difference between the transition metal (Y → Mo) and carbon, which are strongly correlated with the structural properties.[57,58] YC_2 has the highest electronegativity difference (1.33 on the Pauling scale), while MoC_2 possesses the lowest (0.39 on the Pauling scale), the angles of M–C–M ($\angle\theta_{M-C-M}$) gradually decrease, resulting in an increase in the d_{C-C} and thickness of 2D MC_2 from Y to Mo (Fig. S3†). Note that the C–C distances of C_2 dimers are in the range of 1.30–1.37 Å, which are shorter than that in the Ti_8C_{12} cage and MXenes with the C–C distances in the range of 1.40–3.35 Å,[59–61] implying stronger C–C bonding in C_2 dimers.

Table 1 The lattice constants (a and b, in Å), C–C bond length (bond-I, in Å), M–C bond length (bond-II along the x axis and bond-III along the y axis, in Å), bond angle ($\angle\theta_{C-M-C}$), thickness (h, Å) and cohesive energy (E_{coh}, in eV per atom) of the MC_2 (M = Y, Zr, Nb, and Mo) monolayers

System	a	b	Bond-I	Bond-II	Bond-III	$\angle\theta_{C-M-C}$	h	E_{coh}
YC_2	5.77	4.45	1.30	2.39	2.51	138.14°	1.81	−7.40
ZrC_2	5.31	3.92	1.34	2.21	2.33	128.23°	2.07	−7.99
NbC_2	4.96	3.54	1.34	2.08	2.26	119.74°	2.26	−7.98
MoC_2	4.84	3.03	1.37	2.03	2.27	119.28°	2.60	−7.48

3.2 Stabilities of the MC_2 (M = Y, Zr, Nb, and Mo) monolayers

Prior to exploring the physical properties and evaluating the probability of experimental synthesis of the MC_2 (M = Y, Zr, Nb, and Mo) monolayers, we firstly verified their thermodynamic, dynamic, thermal, and mechanical stabilities and investigated the underlying mechanisms for their stabilities.

First, we examined the thermodynamic stability by calculating their cohesive energy (E_{coh}), which is defined as $E_{coh} = (E_{MC_2} - nE_M - mE_c)/(n + m)$, in which E_{MC_2} and E_M/E_c are the energies of the MC_2 monolayer and a free M/C atom, respectively, and n/m is the number of M/C atoms in one unit cell. According to this definition, a more negative E_{coh} value indicates a better thermodynamic stability of the structure. The computed E_{coh} values for MC_2 (M = Y, Zr, Nb, and Mo) monolayers are −7.40, −7.99, −7.98, and −7.48 eV per atom, respectively, lower than that of the TiC_2 monolayer (−6.59 eV),[37] VC_2 monolayer (−7.15 eV),[38] ScC_2 monolayer (−6.33 eV),[42] and the synthesized Ti_2C[62] (6.18 eV per atom) MXene, all of which are demonstrated to be structurally and thermodynamically stable according to the first principles calculations or experimentally. Thus, the four MC_2 (M = Y, Zr, Nb, and Mo) monolayers have solid thermodynamic stability.

Second, the dynamic stability of the MC_2 (M = Y, Zr, Nb, and Mo) monolayers was evaluated by calculating their phonon dispersions, which are shown in Fig. S4.† All of them are dynamically stable as confirmed by the absence of imaginary phonon modes in the entire Brillouin zone. In particular, the highest frequencies for the dynamically stable monolayers (40.25–49.59 THz) are higher or comparable to those of the ScC_2/ScN_2 monolayer (50/38 THz),[42] VC_2 (~43 THz),[38] and the recently proposed TaC_2 monolayer (42 THz),[40] suggesting strong M–C bonding in these MC_2 nanosheets.

Third, FPMD simulations were performed to assess their thermal stability at room temperature (300 K), and the structures after annealing at 300 K for 5 ps are presented in Fig. S5a–d.† Neither bond breakage nor structural distortion can be noted, and then we conclude that the YC_2, ZrC_2, NbC_2 and MoC_2 monolayers possess excellent thermal stabilities at room temperature.

Finally, we assessed the mechanical stability of the MC_2 (M = Y, Zr, Nb, and Mo) monolayers by calculating their elastic constants using the finite distortion method.[63] Mechanically, a stable 2D structure should meet the Born–Huang criteria[64,65] given by $C_{11}C_{22} - C_{12}^2 > 0$ and $C_{66} > 0$. The calculated values of elastic constants fully satisfy these criteria (shown in Table 2), demonstrating that the MC_2 (M = Y, Zr, Nb, and Mo) monolayers are also mechanically stable.

To gain insights into the bonding nature and stabilizing mechanism, we calculated the electron localization functions

Table 2 The elastic constants C_{11} and C_{22} (in N m^{-1}), in-plane Young's modulus Y_x and Y_y (in N m^{-1}), and Poisson's ratio of the TiC_2, YC_2, ZrC_2, NbC_2, and MoC_2 sheets

System	C_{11}	C_{12}	C_{22}	C_{66}	Y_x	Y_y	ν_x	ν_y
YC_2	79.33	22.17	32.21	16.51	64.07	26.01	0.69	0.28
ZrC_2	107.71	34.95	49.15	27.00	82.86	37.81	0.71	0.32
NbC_2	158.97	40.90	55.50	42.85	128.82	44.98	0.74	0.26
MoC_2	180.44	43.76	82.01	47.97	157.09	71.40	0.53	0.24
TiC_2 (ref. 37)	140.58	25.10	70.52	16.19	131.17	66.04	0.59	0.21

(ELFs) of MC_2 (M = Y, Zr, Nb, and Mo) monolayers. The ELF is an effective tool for characterizing chemical bonding and can reflect the electron localization in the system.[66] Generally, the ELF value near zero (blue) denotes a low electron density area, whereas the ELF values of 1.0 (red) and 0.5 (green) represent the perfect localization and the free electron-gas, respectively. As shown in Fig. S6,† in the ELF maps of the (001) and (010) slices we can see that the region between M and C atoms in all the MC_2 monolayers is in the green color corresponding to an ELF of around 0.5, indicating fully delocalized electron distribution, which well shared and delocalized electrons make robust connection between the M and C atoms, and the Bader charge analysis revealed that the each M (M = Y, Zr, Nb, and Mo) atom transfers 1.85, 1.81, 1.73, and 1.15 e$^-$ per atom to the C_2 dimer, respectively, similar to the value of 1.80/1.50 e$^-$ for TiN_2/C_2,[37] 1.74/1.71 e$^-$ for ScC_2/N_2,[42] and 1.85 e$^-$ for YN_2 (ref. 67) monolayers, indicating ionic interactions between M and C atom. While, the C_2 dimer exhibits strong covalent bond characteristics, the results are in agreement with previous studies that the formation of the C_2 dimer plays an important role in stabilizing metal 2D structures. As a consequence, the coexistence of ionic and covalent bonding is mainly responsible for the structural stability.

3.3 Mechanical and electronic properties of the MC_2 (M = Y, Zr, Nb, and Mo) monolayers

Having confirmed the stability of the MC_2 (M = Y, Zr, Nb, and Mo) monolayers, the mechanical properties, including Young's modulus $Y(\theta)$ and Poisson's ratio $\nu(\theta)$, were investigated. The angle-dependent in-plane $Y(\theta)$ and $\nu(\theta)$ were estimated by using the following equation:[68]

$$Y(\theta) = \frac{C_{11}C_{22} - C_{12}^2}{C_{11}\sin^4\theta + A\sin^2\theta\cos^2\theta + C_{22}\cos^4\theta} \quad (1)$$

$$\nu(\theta) = \frac{C_{12}\sin^4\theta - B\sin^2\theta\cos^2\theta + C_{12}\cos^4\theta}{C_{11}\sin^4\theta + A\sin^2\theta\cos^2\theta + C_{22}\cos^4\theta} \quad (2)$$

where $A = (C_{11}C_{22} - C_{12}^2)/C_{66} - 2C_{12}$ and $B = C_{11} + C_{12} - (C_{11}C_{22} - C_{12}^2)/C_{66}$.

Based on the above equations, we plotted $Y(\theta)$ and $\nu(\theta)$ with the variation of angle θ (Fig. 2). The $Y(\theta)$ of Y/Zr/Nb/MoC_2 monolayers decreases from a maximum value of 64.07/82.86/128.82/157.09 N m^{-1} along the x direction to a minimum value of 26.01/37.81/44.98/71.40 N m^{-1} along the y direction, reflecting their high mechanical anisotropy. However, the $Y(\theta)$ of the TiC_2 monolayer decreases from a maximum value of 131.17 N m^{-1} in the x direction to a minimum value of 55 N m^{-1} at about $\theta = 46°$, which is consistent with a previous report.[37] Compared with other well-known 2D materials, strikingly, our calculated Y along x and y directions of these C_2-containing monolayers are comparable to the value of MoS_2 (122 N m^{-1}),[69] silicene (61.7 N m^{-1}) and germanene (44 N m^{-1}),[70] but smaller than that of graphene (341.60 N m^{-1})[71] and hexagonal h-BN (271 N m^{-1}),[72] implying high flexibility for these monolayers. The modest mechanical properties are beneficial for the charge–discharge process of rechargeable ion batteries.

To analyze the electronic properties of the MC_2 (M = Y, Zr, Nb, and Mo) monolayers, the atom-projected electronic band structure and partial density of states (PDOS) were carefully investigated (as shown in Fig. 3 and S7†). The results showed that all considered monolayers exhibit metallic character, as indicated by the partially occupied bands crossing the Fermi level in the Brillouin zone. The orbital analysis suggested that the bands near the Fermi level are dominated by the M_d orbitals, while the C_p orbitals make minor contribution by hybridizing with the M–d states, which is in line with the electrons transferred from M to C atoms based on the Bader charge analysis, as shown in Fig. S6.† The metallic nature of MC_2 (M =

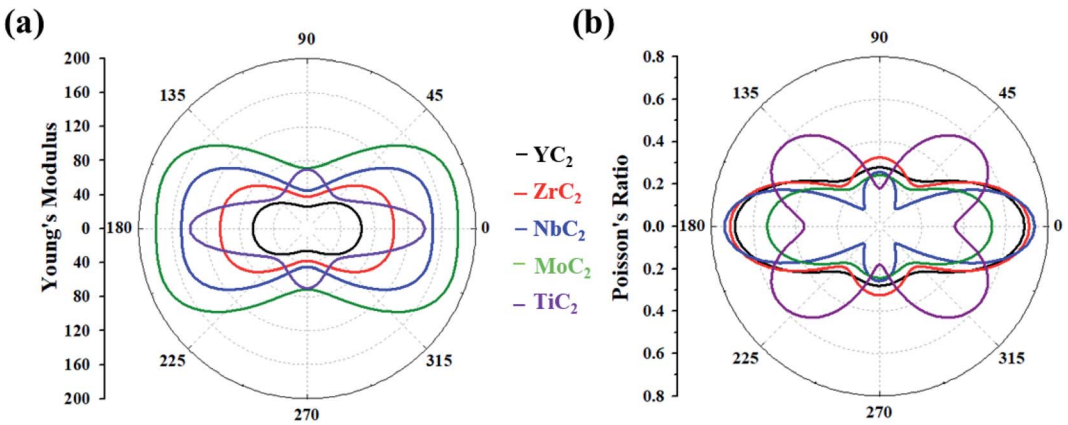

Fig. 2 (a) Young's modulus and (b) Poisson's ratio of the MC_2 (M = Y, Zr, Nb, Mo and Ti) monolayers as a function of the in-plane angle θ, and θ = 0° corresponds to the x-axis.

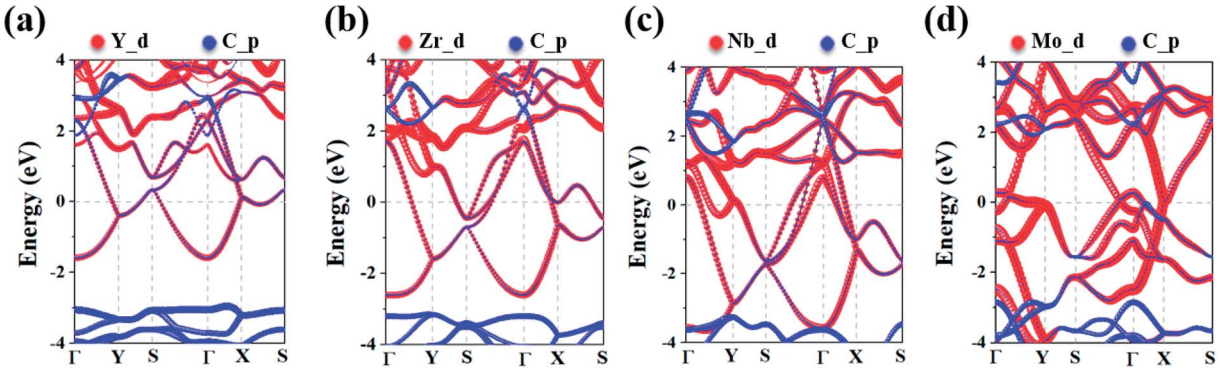

Fig. 3 The electronic band structures of the (a) YC_2, (b) ZrC_2, (c) NbC_2, and (d) MoC_2 monolayers. The red and blue curves denote the d orbits of the metal atoms and the p orbits of C atoms, respectively. The Fermi energy is denoted by a dashed line at 0 eV.

Y, Zr, Nb, and Mo) monolayers indicates the advantage in electrical conductivity, which is highly desirable for high performance of electrode materials.

3.4 Na adsorption and diffusion on the MC_2 (M = Y, Zr, Nb, and Mo) monolayers

The development of sodium ion batteries (SIBs) is often hindered by the limited choice of anode materials. The modest mechanical properties and metallic feature of the examined MC_2 (M = Y, Zr, Nb, and Mo) monolayers facilitate our investigation on their potential application as SIB anode materials.

The adsorption behavior between metal atoms and 2D materials closely correlates with the anode performance. Thus, we firstly examined the energy-preferred adsorption sites for a single Na atom on the surface of MC_2 (M = Y, Zr, Nb, and Mo) monolayers with a $2 \times 2 \times 1$ supercell. Four high symmetry adsorption sites were considered, namely A_1 (where Na sits over the midpoint of the bottom C–C bond), A_2 (where Na sits over the midpoint of the top C–C bond), A_3 (where Na sits over the M atom and interacts with four top C atoms) and A_4 (where Na sits over the M atom and interacts with two top C atoms) sites, as shown in Fig. 1a. After full relaxation, the energetically most favorable adsorption sites for Na on MC_2 (M = Y, Zr, Nb, and Mo) monolayers were identified by calculating their adsorption energy (E_{ads}), which is defined as:

$$E_{ads} = E_{tot} - E_{MC_2} - E_{Na} \quad (3)$$

where E_{tot} and E_{MC_2} are the energies of the MC_2 supercell with and without a single Na atom, respectively, and E_{Na} represents the energy of an isolated Na atom. According to this definition, a more negative adsorption energy indicates a more favorable exothermic reaction between the MC_2 monolayer and Na atom.

Almost all the investigated MC_2 monolayers can effectively adsorb Na atoms, as indicated by the negative E_{ads} values (Fig. 4). Except for the YC_2 monolayer, on which the most stable adsorption site of Na is the A_3 site ($E_{ads} = -1.55$ eV), the Na's energy-favorable site on the other three MC_2 (M = Zr, Nb, and Mo) monolayers is A_1 with an E_{ads} of −1.67, −2.45 and −2.95 eV, respectively, in agreement with the preferred adsorption site on TiC_2 (A_1),[37] VC_2 (A_1),[38] and ScC_2 (A_3).[42] In addition, the A_1 (A_3 and A_4) site is the Na's second favorable adsorption site on the YC_2 (ZrC_2/NbC_2 and MoC_2) monolayer. The difference of the most preferred Na adsorption site is due to the shorter Na–C bond lengths (d_{Na-C}) formed between Na and C at the A_3 (A_1) site than those at the A_1 (A_3) site on YC_2 (ZrC_2, NbC_2, and MoC_2): 2.51 *vs.* 3.54/3.70 Å (2.53 *vs.* 2.61, 2.59 *vs.* 2.62, and 2.78 *vs.* 2.81 Å). Among the four examined monolayers, Na has the strongest/weakest interaction with the MoC_2/YC_2 monolayer, which can be understood by the gradually increasing distance between the adsorbed Na and the MC_2 monolayer (from 1.49 Å on MoC_2 to 1.64 Å on YC_2, as shown in Fig. 5).

Fig. 5 presents the fully optimized structures for the Na-adsorbed YC_2 monolayer at the site A_3 and MC_2 (M = Zr, Nb, and Mo) monolayers at the site A_1, respectively. For Na-adsorbed Y/Zr/Nb/MoC_2 monolayers, the Na–C bond length is 2.51/2.53/2.59/2.78 Å, and the adsorption height (h), *i.e.*, the vertical distance between the top-layer carbon and Na atom is 1.64/1.58/1.54/1.49 Å. Obviously, the MC_2 monolayer with a larger atomic number (smaller atomic radii) from Y → Mo has a lower adsorption height (h); however, the Na–C bond length

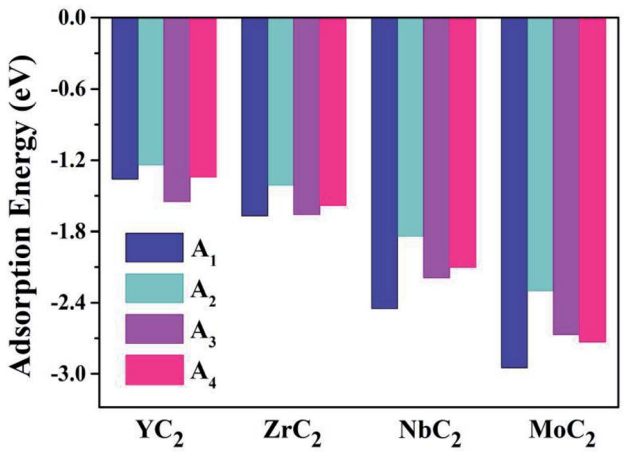

Fig. 4 The adsorption energies of a single Na atom on the (M = Y, Zr, Nb, and Mo) monolayer at the four examined adsorptions sites A_1, A_2, A_3 and A_4.

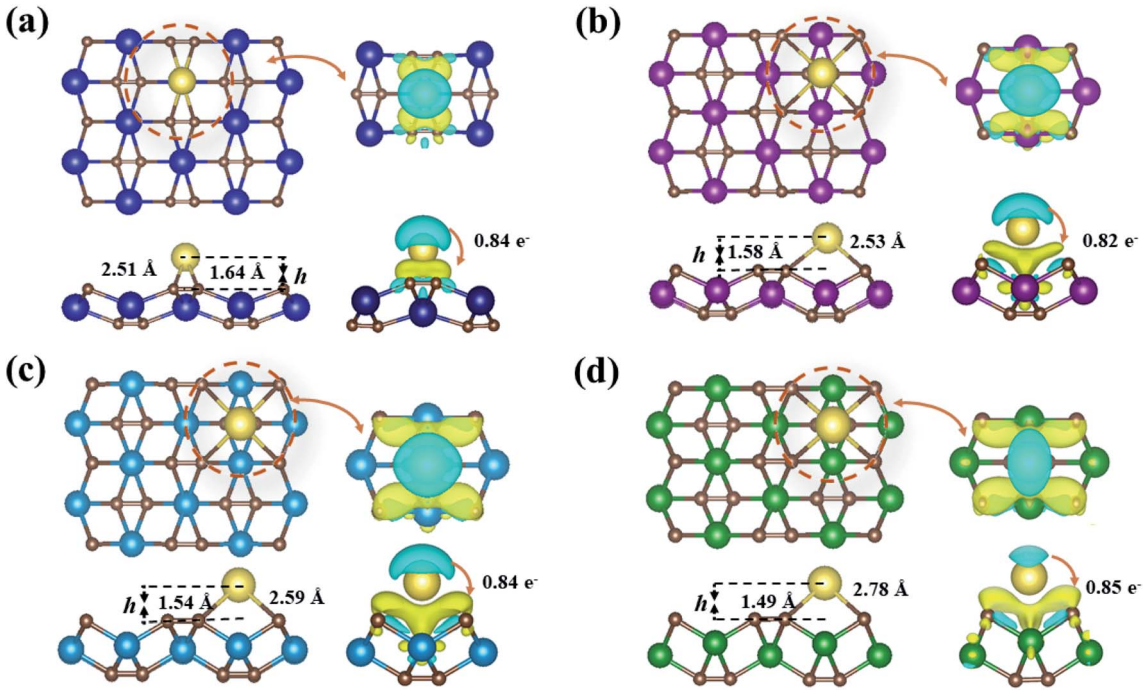

Fig. 5 Top and side views of the most stable Na-adsorbed configurations of YC_2 (a), ZrC_2 (b), NbC_2 (c), and MoC_2 (d) monolayers; right plane corresponds to the charge density difference. The isosurface level is set to 0.002 e $Å^{-3}$. Blue and yellow regions indicate electron depletion and accumulation, respectively.

and adsorption energy (E_{ads}) are inversely proportional to the atomic radii.

To better understand the physical mechanism of the adsorption process, we investigated the charge transfer process between a single Na atom adsorbed on the MC_2 (M = Y, Zr, Nb, and Mo) monolayers by using the charge density difference using the following formula,

$$\Delta\rho = \rho_{tot} - \rho_{MC_2} - \rho_{Na} \quad (4)$$

where ρ_{tot} and ρ_{MC_2} denote the total electron densities of the relaxed MC_2 monolayer with and without Na, respectively, and ρ_{Na} is the total electron density of an isolated Na atom. Fig. 5 right panel presents charge density difference plots for Na adsorbed YC_2 at site A_3 and Zr/Nb/MoC_2 at site A_1, in which the electron accumulation (yellow) is located between the Na atom and MC_2 monolayer, while the electron depletion (blue) is around the Na atoms, suggesting that the Na donates electrons and the MC_2 monolayer accepts electrons, which originates from the smaller electronegativity of Na than that of C and metal atoms M (M = Y, Zr, Nb, and Mo). The Bader charge analysis showed that the electrons transferred from Na to the MC_2 (M = Y, Zr, Nb, and Mo) monolayers are 0.84, 0.82, 0.84, and 0.85 e^-, respectively. It can also be observed from the PDOS of Na-adsorbed MC_2 (M = Y, Zr, Nb, and Mo) shown in Fig. S8† that hybridization exists between the Na atom and the C atom of the MC_2 (M = Y, Zr, Nb, and Mo) monolayer. At the same time, the adsorption of Na only slightly influences the electronic structure of the pristine MC_2 monolayer, and the metallic features are maintained after the adsorption of Na according to Fig. S8,† which is rather beneficial to their application as anode materials.

Metal mobility was another significant factor in the design and selection of effective anode materials, which are directly linked to the charge–discharge rates of rechargeable batteries. Thus, we further investigated the diffusion of Na on the MC_2 (M = Y, Zr, Nb, and Mo) monolayers (Fig. 6). For the YC_2 monolayer (Fig. 6b), since A_3 is the energetically most favorable site among the four adsorption sites (A_1, A_2, A_3, and A_4), three representative possible diffusion pathways were considered: path-I (A_3–A_1–A_3), where Na migrates from an A_3 to another A_3 by crossing an A_1 site, marked by red arrows; path-II (A_3–A_4–A_3), where Na migrates from an A_3 to another A_3 by crossing an A_4 site, marked by blue arrows; path-III (A_3–A_2–A_3), where Na migrates from an A_3 to another A_3 by crossing an A_2 site, marked by black arrows. For the Zr/Nb/MoC_2 monolayers (Fig. 6d, f and h), similarly, there are three diffusion pathways with both starting and ending sites at A_1: path-I (A_1–A_3–A_1), path-II (A_1–A_2–A_1), and path-III (A_1–A_4–A_1), marked by red, blue and black arrows, respectively.

The energy profiles for Na diffusion over MC_2 (M = Y, Zr, Nb, and Mo) monolayers along the examined diffusion pathways are illustrated in Fig. 6a, c, e and g. Obviously, Na diffusing along path-I has the lowest diffusion barrier (E_d) on the YC_2 (E_d = 0.21 eV), ZrC_2 (E_d = 0.04 eV), and NbC_2 (E_d = 0.20 eV) monolayers, while on the MoC_2 monolayer, path-III has the smallest diffusion barrier of 0.22 eV. Actually, the energy-favored diffusion route is Na migration from the most energy-preferred site to another crossing the second energy-preferred site on the four

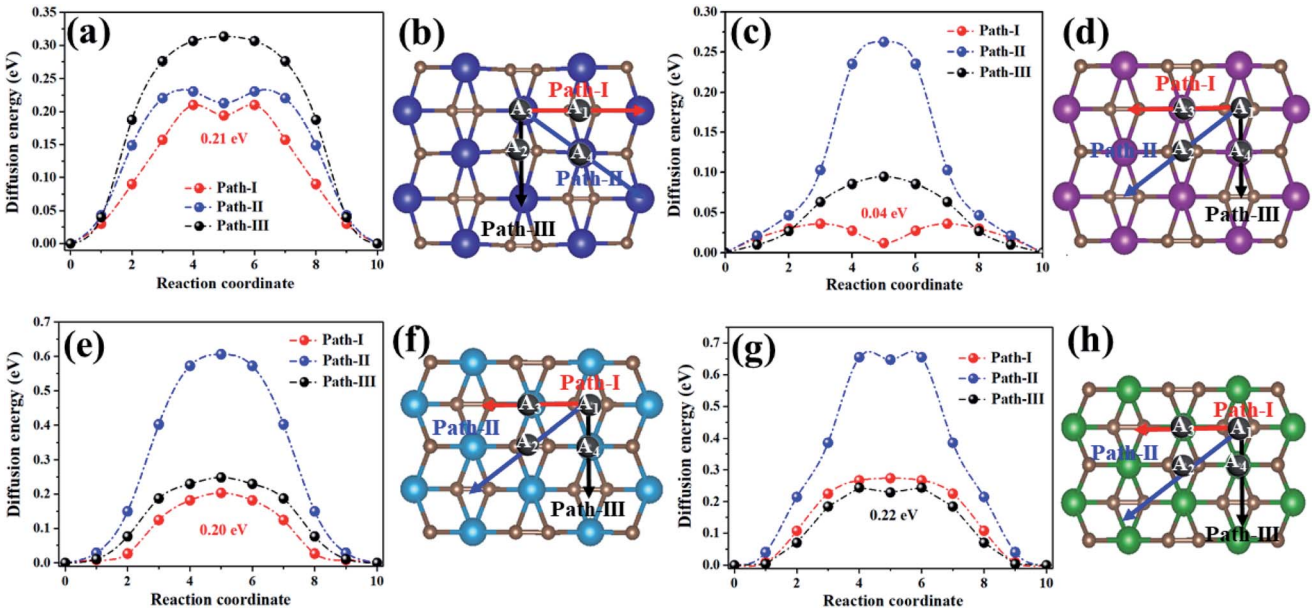

Fig. 6 The energy profile (left plane) and diffusion pathways (right plane) of Na diffusing on theYC_2 (a and b), ZrC_2 (c and d), NbC_2 (e and f), and MoC_2 (g and h) monolayers.

monolayers. Since the second lowest adsorption site on MoC_2 is A_4, the Na diffusion path with the smallest barrier is path-III instead of path-I on the other three monolayers. The corresponding diffusion lengths of Na along the minimum energy pathways on the four MC_2 monolayers are given in Fig. S9,† and the diffusion length of Na on MC_2 monotonically increases with the lattice constant from the MoC_2 to the YC_2 monolayer. Note that the Na diffusion barriers on the four MC_2 monolayers are all lower than that on borophene (0.32 eV),[73] Ti_3C_4 (0.35)[74] and MoS_2 (0.28 eV),[75] and the lowest E_d value of 0.04 eV on the ZrC_2 monolayer is comparable with the E_d on ScC_2 (0.05 eV)[42] and Ti_3C_2 (0.096),[76] as shown in Table 3, indicating their excellent charge–discharge rate. Compared with the reported TiC_2 monolayer as a promising anode for LIBs,[37] the Na diffusing along path-I has the lowest diffusion barrier on TiC_2 (E_d = 0.19 eV, Fig. S10†), and the E_d is comparable with the values on Y/Nb/MoC_2 monolayers (0.20–0.22 eV), but higher than that on the ZrC_2 monolayer (0.04 eV). Thus, as for SIB anode materials, compared to the TiC_2 monolayer, ZrC_2 distinguishes itself among the four examined MC_2 (M = Y, Zr, Nb, and Mo) monolayers, since it has the lowest Na diffusion barrier and high Na capacity comparable to that of TiC_2. Overall, from the perspective of Na diffusion behavior, anode materials with low energy barriers and short diffusion pathway lengths are suitable for SIBs.

Table 3 Summary of the theoretical specific capacity (in mA h g^{-1}) and diffusion barriers (in eV) of some widely investigated promising electrode materials for SIBs

	Theoretical specific capacity	Diffusion barrier	References
YC_2	478	0.21	This work
ZrC_2	699	0.04	This work
NbC_2	687	0.20	This work
MoC_2	675	0.22	This work
TiC_2	727	0.19	This work
Ti_3C_2	352	0.096	78
Ti_3C_4	560	0.35	74
ScC_2	777	0.05	42
Sc_2C	362	0.012	81
Nb_2C	271	0.015	33
Mo_2C	132	0.015	34
MoC	284.2	0.09	82
MoS_2	146	0.28	75
Phosphorene	315.52	0.30	80
$Na_2Mn_3O_7$	166.1	0.16	7

3.5 Theoretical storage capacity and open-circuit voltage

2D materials as anode materials display a lot of attractive properties; besides mechanical flexibility, excellent electrical conductivity, and lower diffusion energies, they also have the ability to adsorb multilayer Na atoms and exhibit high capacity.[77,78] Inspired by these properties, we expect that the predicted MC_2 (M = Y, Zr, Nb, and Mo) monolayers can be used as anodes for SIBs with high storage capacity. Here, the two important descriptors, namely storage capacity (C) and average open-circuit voltage (OCV), were calculated to determine the performance of the SIBs based on the charge–discharge mechanism.

The OCV can be evaluated from the following common half-cell reaction of the charge/discharge process:

$$MC_2 + xNa^{n+} + xne^- \leftrightarrow Na_xMC_2 \quad (5)$$

when the volume and entropy effects during the sodiation process were neglected, the open-circuit voltage (OCV) can be derived from the average adsorption energy (E_{ave}) as:

$$\mathrm{OCV} = -E_{\mathrm{ave}}/xne \tag{6a}$$

$$E_{\mathrm{ave}} = (E_{\mathrm{Na}_x\mathrm{MC}_2} - E_{\mathrm{MC}_2} - xE_{\text{Na-bulk}})/x \tag{6b}$$

where E_{MC_2}, $E_{\mathrm{Na}_x\mathrm{MC}_2}$, and $E_{\text{Na-bulk}}$ are the energy of the pristine MC_2 monolayer, the total energy of Na adsorbed MC_2, and the energy per Na atom in the sodium bcc bulk, respectively, n is the number of valence electrons ($n = 1$ for Na), and x is the chemical content of sodium atoms; ideally, the anode material can keep adsorbing Na atoms if E_{ave} is smaller than 0 eV per atom. The corresponding maximum capacity were calculated by using the following equation:

$$C = x_{\max} \times F/M_{\mathrm{MC}_2} \tag{7}$$

where $x_{\max}$ is the highest concentration of Na in Na_xMC_2, F is the Faraday constant (26 801 mA h mol^{-1}), and M_{MC_2} is the molar weight of MC_2 (M = Y, Zr, Nb, and Mo).

Then the maximum storage capacity of Na atoms on MC_2 (M = Y, Zr, Nb, and Mo) monolayers was evaluated by adding Na atoms to the surface gradually. As mentioned above, the most stable adsorption sites for Na on the four monolayers have been determined: the first layer of Na interaction at the A_3 site for YC_2 and the A_1 site for Zr/Nb/MoC_2, respectively; when the adsorption positions of the first layer are completely occupied, the subsequently added Na atoms form a second and a third adsorption layer. In addition, for the different sodium concentrations on the MC_2 monolayer, the most stable configurations for each concentration, we considered by calculating their formation energy (E_f) of Na_xMC_2 (M = Y, Zr, Nb, and Mo) compounds with respect to the MC_2 monolayer and Na bulk phase as the references (Fig. S11†).[79]

Here, based on the MC_2 monolayer, taking the process of successive adsorption of Na atoms on the NbC_2 monolayer as an example, adding a Na atom at site A_1 on one surface of NbC_2 results in a low-limit chemical formula Na_xNbC_2 ($x = 0.125$, Fig. 5c). Our computations showed that Na atoms tend to bond to both surfaces of the NbC_2 monolayer when occupying the A_1 site (Fig. S12–S14†). When the A_1 sites of both surfaces were all occupied, Na atoms start to occupy the A_3 sites in the second layer (Fig. S15†). Thus, the several possible configurations with both surfaces exposed to Na atoms were carefully considered for Na_xNbC_2 systems with higher x values ($x = 0.25$, 0.375, 0.5, 1, 2, 3), and the most stable configurations for each concentration are shown in Fig. 7a–f. The same approach was used to construct Na_xYC_2, Na_xZrC_2, and Na_xMoC_2 systems.

The average adsorption energy decreases with the increase of Na concentration (x), indicating the decreased thermodynamic stability of Na_xMC_2 (Fig. 7g), which can be attributed to the repulsive interaction between Na atoms, thus making more adsorption more difficult. For the Zr/Nb/MoC_2 monolayer, the first Na-adsorption layer is formed by placing Na at the most favorable sites (A_1) on both sides with an E_{ave} of −0.41/−0.77/−0.65 eV (the composite is $NaZrC_2$/$NaNbC_2$/$NaMoC_2$), suggesting the feasibility of adsorbing the second Na layer. The E_{ave} of the second Na layer with Na adsorbing at site A_3 (A_4 for MoC_2) is −0.27/−0.32/−0.28 eV and the corresponding configurations are Na_2ZrC_2, Na_2NbC_2, and Na_2MoC_2. When adding the third Na-layer on both sides with site A_4 (A_3 for MoC_2), the E_{ave} is −0.14/−0.25/−0.24 eV and the composites are Na_3ZrC_2,

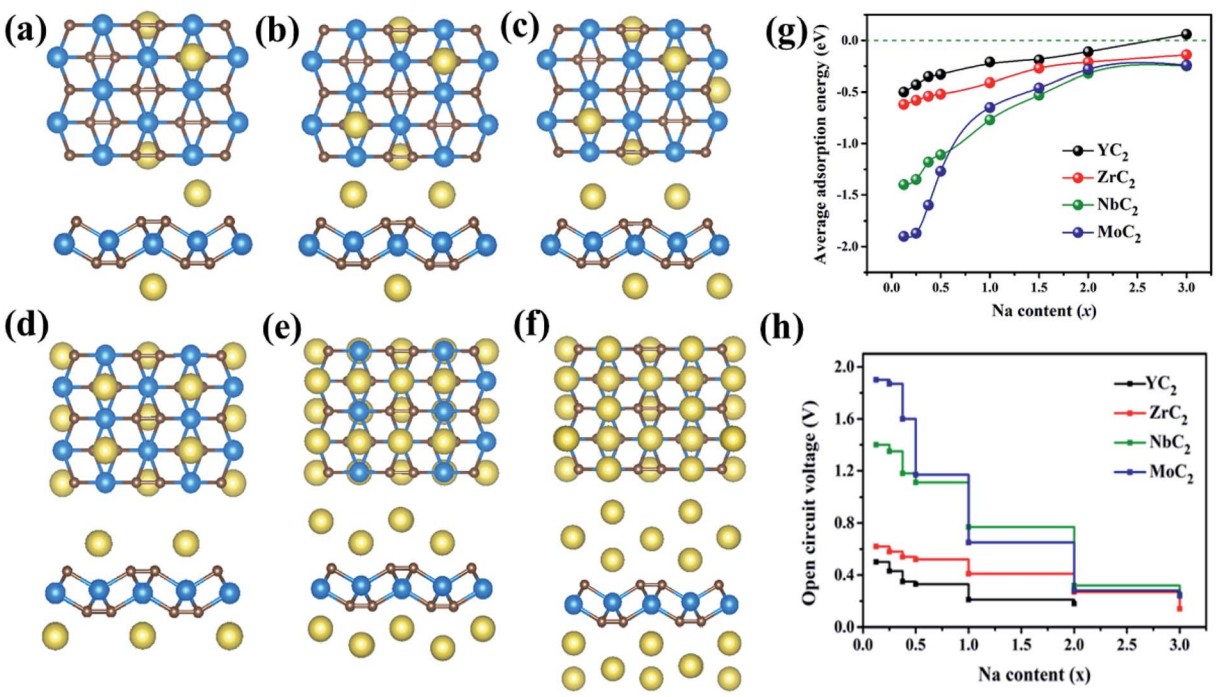

Fig. 7 Top and side views of the optimized structures of $Na_{0.25}NbC_2$ (a), $Na_{0.375}NbC_2$ (b), $Na_{0.5}NbC_2$ (c), $NaNbC_2$ (d), Na_2NbC_2 (e), and Na_3NbC_2 (f). The average adsorption energy (g) and open circuit voltage profile (h) of Na_xYC_2, Na_xZrC_2, Na_xNbC_2, and Na_xMoC_2 as a function of Na concentration.

Na_3ZrC_2, and Na_3MoC_2. However, for the YC_2 monolayer, in the first Na-layer Na atoms are adsorbed at the most favorable sites (A_3) on both sides, and the E_{ave} is −0.21 eV (the chemical formula is $NaYC_2$). The E_{ave} of the second layer with Na atoms locating at site A_1 is −0.11 eV and the corresponding configuration is Na_2YC_2. The third Na-layer with Na atom adsorption at site A_4 on both sides has an E_{ave} of 0.06 eV, which implies that only the two adsorption layers of Na atoms are stable on the YC_2 monolayer. Thus, we can conclude that the three (two) layers of Na atoms can be stably adsorbed on the Zr/Nb/MoC_2 (YC_2) monolayer.

Based on the above results, we estimated the maximum capacity (C) and open-circuit voltage (OCV) of Na atoms adsorbed on the MC_2 (M = Y, Zr, Nb, and Mo) monolayers with the chemical stoichiometry of Na_2YC_2, Na_3ZrC_2, Na_3NbC_2, and Na_3MoC_2 (Fig. 7h). The corresponding values of maximum capacity (C) for SIBs are 478, 699, 687, and 675 mA h g^{-1}, respectively. The MC_2 (M = Y, Zr, Nb, and Mo) monolayers have much larger theoretical specific capacity in comparison to other electrode materials for SIBs, such as Ti_3C_2 (352 mA h g^{-1}),[76] phosphorene (315.52 mA h g^{-1}),[80] Sc_2C (362 mA h g^{-1}),[81] Nb_2C (271 mA h g^{-1}),[33] MoS_2 (146 mA h g^{-1}),[75] MoC (248.2 mA h g^{-1})[82] and Na-based layered materials ($Na_2Mn_3O_7$, 166.1 mA h g^{-1}),[7] as shown in Table 3. We also estimated the Na capacity on the TiC_2 monolayer and found that the TiC_2 monolayer can adsorb two Na layers with the final formula of Na_2TiC_2, and the corresponding maximum specific capacity was then determined to be 727.29 mA h g^{-1}, higher than that of the Y/Zr/Nb/MoC_2 monolayer. Thus, as for SIB anode materials, compared to the TiC_2 monolayer, ZrC_2 distinguishes itself among the four examined MC_2 (M = Y, Zr, Nb, and Mo) monolayers, since it has the lowest Na diffusion barrier and high Na capacity comparable to that of TiC_2.

In addition, the OCV values are 0.11, 0.18, 0.25 and 0.24 V, which can avoid the dendrite formation of Na metal during the charge–discharge process due to satisfying the requirement of 0.1–1.0 eV for SIB anode materials.[83] At the same time, the values are rather low and comparable to or slighter larger than that of 2D materials Mo_2C (0.166 V),[34] Ti_3C_2 (0.137 V),[78] and NiC_3 (0.17 V).[84] The OCV values are low for Na atoms to be adsorbed on MC_2 (M = Y, Zr, Nb, and Mo) nanosheets, which are beneficial for increasing and operating voltage and safety in practical applications.

Then, we examined the geometries of the MC_2 (M = Y, Zr, Nb, and Mo) monolayers upon Na adsorption to evaluate the expansion in volume. The changes of the lattice constant and volume for the host sheets with interacted Na atoms are listed in Table S1.† Compared with the bare sheets, the expansions of the lattice and volume for the maximum Na concentrations are less than 8% and 10%, respectively, comparable to or much smaller than the lattice changes of the FeSe monolayer (5.50%)[71] and the volume expansion of graphite (10%)[85] and Na-based bulk electrode material $NaTiF_4$ (13%),[7] implying good cycling stability.

Finally, we explored the stability of the examined four C_2-containing MC_2 (M = Y, Zr, Nb, and Mo) monolayers under high concentration Na adsorption, by carrying out the FPMD stimulations of Na_2YC_2, Na_3ZrC_2, Na_3NbC_2, and Na_3MoC_2 monolayers for 5 ps at 300 and 500 K, respectively. No bond breakage or atomic structure reconstruction was observed, indicating that the 2D MC_2 (M = Y, Zr, Nb, and Mo) materials are still stable under the maximum coverage of sodium. Overall, we conclude that the good structural stability of MC_2 (M = Y, Zr, Nb, and Mo) sheets endows them with great potential as high-performance anode materials for SIBs.

4. Conclusions

In summary, based on first-principles calculations, we proposed four C_2-containing monolayers (MC_2, M = Y, Zr, Nb, and Mo) and systematically investigated the structural stability, mechanical and electronic properties, as well as the performance as anode materials for SIBs. Our results show that the MC_2 (M = Y, Zr, Nb, and Mo) monolayers possess high cohesive energy and good dynamic, thermal and mechanical stability, and have metallic properties with excellent electronic conductivities. When used as battery electrodes for adsorbing Na atoms, the YC_2 and Zr/Nb/MoC_2 monolayers can adsorb two and three layers of Na atoms with the final formula of Na_2YC_2 and Na_3ZrC_2/Na_3NbC_2/Na_3MoC_2, respectively, and the corresponding maximum specific capacities (open circuit-voltage) were calculated to be 478 (0.11) and 699 (0.18)/687 (0.25)/675 (0.24) mA h g^{-1} (V), respectively. Taking advantage of containing C_2 dimers, the MC_2 (M = Y, Zr, Nb, and Mo) monolayers show superior stability and have high Na capacity due to the higher content of C. In addition, Na atoms show fast diffusion on the MC_2 (M = Y, Zr, Nb, and Mo) monolayers with low diffusion barriers (0.21, 0.04, 0.20 and 0.22, respectively), indicating excellent rate capability. In view of the superior properties, such as good electronic conductivity, fast Na diffusion, low OCV, and high theoretical Na storage capacity, MC_2 (M = Y, Zr, Nb, and Mo) monolayers become promising anode materials for SIBs.

Conflicts of interest

There are no conflicts of interest to declare.

Acknowledgements

This work was supported by the National Natural Science Foundation of China (11964024), the "Grassland Talents" project of Inner Mongolia autonomous region (12000-12102613), the Young Scientific Talent Development Project (10000-21221505) and the Training Program of Innovation and Entrepreneurship for Undergraduates of Inner Mongolia University (201812236).

References

1 B. Scrosati, *Electrochim. Acta*, 2000, **45**, 2461–2466.
2 V. Etacheri, R. Marom, R. Elazari, G. Salitra and D. Aurbach, *Energy Environ. Sci.*, 2011, **4**, 3243–3262.

3 E. Fan, L. Li, Z. Wang, J. Lin, Y. Huang, Y. Yao, R. Chen and F. Wu, *Chem. Rev.*, 2020, **120**, 7020–7063.
4 R. S. Carmichael, *Practical Handbook of Physical Properties of Rocks and Minerals*, CRC Press, Boca Raton, FL, 1989.
5 N. Yabuuchi, K. Kubota, M. Dahbi and S. Komaba, *Chem. Rev.*, 2014, **114**, 11636–11682.
6 V. Palomares, P. Serras, I. Villaluenga, K. B. Hueso, J. Carretero-González and T. Rojo, *Energy Environ. Sci.*, 2012, **5**, 5884–5901.
7 X. Zhang, Z. Zhang, S. Yao, A. Chen, X. Zhao and Z. Zhou, *npj Comput. Mater.*, 2018, **4**, 13.
8 D. Kundu, E. Talaie, V. Duffort and L. F. Nazar, *Angew. Chem., Int. Ed.*, 2015, **54**, 3431–3448.
9 Y. Wen, K. He, Y. Zhu, F. Han, Y. Xu, I. Matsuda, Y. Ishii, J. Cumings and C. Wang, *Nat. Commun.*, 2014, **5**, 4033.
10 P. Ge and M. Fouletier, *Solid State Ionics*, 1988, **28**, 1172–1175.
11 Y. Bahari, B. Mortazavi, A. Rajabpour, X. Zhuang and T. Rabczuk, *Energy Storage Mater.*, 2021, **35**, 203–282.
12 J. Lin, T. Xu, F. Han and G. Yang, *Wiley Interdiscip. Rev.: Comput. Mol. Sci.*, 2020, **10**, 1437.
13 X. Huang, Z. Zeng and H. Zhang, *Chem. Soc. Rev.*, 2013, **42**, 1934–1946.
14 R. Lv, J. A. Robinson, R. E. Schaak, D. Sun, Y. Sun, T. E. Mallouk and M. Terrones, *Acc. Chem. Res.*, 2015, **48**, 56–64.
15 K. Tu, F. Li and Z. Chen, *J. Mater. Res.*, 2016, **31**, 878–885.
16 L. Wang and T. Sasaki, *Chem. Rev.*, 2014, **114**, 9455–9486.
17 F. Li, C. R. Cabrera and Z. Chen, *J. Mater. Chem. A*, 2014, **2**, 19180–19188.
18 J. Jia, Bi. Li, S. Duan, Z. Cui and H. Gao, *Nanoscale*, 2019, **11**, 20307–20314.
19 Z. Guo, J. Zhou and Z. Sun, *J. Mater. Chem. A*, 2017, **5**, 23530–23535.
20 X. Tang, X. Guo, W. Wu and G. Wang, *Adv. Energy Mater.*, 2018, **8**, 1801897.
21 Q. Tang, Z. Zhou and P. Shen, *J. Am. Chem. Soc.*, 2012, **134**, 16909–16916.
22 S. Lei, X. Chen, B. Xiao, W. Zhang and J. Liu, *ACS Appl. Mater. Interfaces*, 2019, **11**, 28830–28840.
23 T. Zhang, Y. Ma, B. Huang and Y. Dai, *ACS Appl. Mater. Interfaces*, 2019, **11**, 6104–6110.
24 S. Karmakar, C. Chowdhury and A. Datta, *J. Phys. Chem. C*, 2016, **120**, 14522–14530.
25 C. S. Liu, X. Yang, J. Liu and X. J. Ye, *ACS Appl. Mater. Interfaces*, 2018, **1**, 3850–3859.
26 M. Naguib, M. Kurtoglu, V. Presser, J. Lu, J. Niu, M. Heon, L. Hultmman, Y. Gogotsi and M. W. Barsoum, *Adv. Mater.*, 2011, **23**, 4248–4253.
27 O. Mashtalir, M. Naguib and V. N. Mochalin, *Nat. Commun.*, 2013, **4**, 1716.
28 D. Er, J. Li, M. Naguib, Y. Gogotsi and V. B. Shenoy, *ACS Appl. Mater. Interfaces*, 2014, **6**, 11173–11179.
29 Y. X. Yu, *J. Phys. Chem. C*, 2016, **120**, 5288–5296.
30 Q. Meng, J. Ma, Y. Zhang, Z. Li, C. Zhi, A. Hu and J. Fan, *Nanoscale*, 2018, **10**, 3385–3392.
31 S. Zhao, W. Kang and J. Xue, *J. Phys. Chem. C*, 2014, **118**, 14983–14990.
32 J. Hu, B. Xu, C. Ouyang, S. A. Yang and Y. Yao, *J. Phys. Chem. C*, 2014, **118**, 24274–24281.
33 J. Hu, B. Xu, C. Ouyang, Y. Zhang and S. A. Yang, *RSC Adv.*, 2016, **6**, 27467–27474.
34 Q. Sun, Y. Dai, Y. Ma, T. Jing, W. Wei and B. Huang, *J. Phys. Chem. Lett.*, 2016, **7**, 937–943.
35 Z. Xu, X. Lv, J. Chen, L. Jiang, Y. Lai and J. Li, *Phys. Chem. Chem. Phys.*, 2017, **19**, 7807–7819.
36 Y. Zhou and X. Zu, *Electrochim. Acta*, 2017, **235**, 167–174.
37 T. Zhao, S. Zhang, Y. Guo and Q. Wang, *Nanoscale*, 2016, **8**, 233–242.
38 J. Xu, D. Wang, R. Lian, X. Gao, Y. Liu, G. Yury, G. Chen and Y. Wei, *J. Mater. Chem. A*, 2019, **7**, 8873–8881.
39 B. Zhang, W. Zhang, Q. Meng, L. Fan and Q. Zhang, *Phys. Chem. Chem. Phys.*, 2019, **21**, 1606–1613.
40 T. Yu, S. Zhang, F. Li, Z. Zhao, L. Liu, H. Xu and G. Yang, *J. Mater. Chem. A*, 2017, **5**, 18698–18706.
41 B. Zhang, Q. Zhang and Y. Bai, *J. Phys.: Condens. Matter*, 2018, **30**, 17.
42 H. Huang, H.-H. Wu, C. Cui, B. Huang and T.-Y. Zhang, *J. Mater. Chem. A*, 2019, **7**, 8897–8904.
43 C. Tang, X. Wang, H. Yao and L. Fu, *Mater. Today Commun.*, 2020, **25**, 101587.
44 T. Zhao, J. Zhou, Q. Wang, Y. Kawazoe and P. Jena, *ACS Appl. Mater. Interfaces*, 2016, **8**, 26207–26212.
45 G. Kresse and J. Hafner, *Phys. Rev. B: Condens. Matter Mater. Phys.*, 1994, **49**, 14251–14269.
46 G. Kresse and J. Hafner, *Phys. Rev. B: Condens. Matter Mater. Phys.*, 1993, **47**, 558–561.
47 K. Albe and J. Furthmüller, *Phys. Rev. B: Condens. Matter Mater. Phys.*, 1996, **54**, 11169–11186.
48 P. E. Blöchl, *Phys. Rev. B: Condens. Matter Mater. Phys.*, 1994, **50**, 17953–17979.
49 J. P. Perdew, K. Burke and M. Ernzerhof, *Phys. Rev. Lett.*, 1996, **77**, 3865–3868.
50 H. J. Monkhorst and J. D. Pack, *Phys. Rev. B: Solid State*, 1976, **13**, 5188–5192.
51 K. Momma and F. Izumi, *J. Appl. Crystallogr.*, 2011, **44**, 1271–1276.
52 A. Togo and I. Tanaka, *Scr. Mater.*, 2015, **108**, 1–5.
53 G. J. Martyna, M. L. Klein and M. Tuckerman, *J. Chem. Phys.*, 1992, **97**, 2635–2643.
54 G. Henkelman and H. Jónsson, *J. Chem. Phys.*, 2000, **113**, 9901–9904.
55 G. Henkelman and H. Jónsson, *J. Chem. Phys.*, 2000, **113**, 9978–9985.
56 G. Henkelman, A. Arnaldsson and H. Jonsson, *Comput. Mater. Sci.*, 2006, **36**, 354–360.
57 N. Li, Y. Li, X. Zhu, C. Huang, J. Kai and J. Fan, *J. Phys. Chem. C*, 2020, **124**, 14978–14986.
58 Y. Li, D. B. Putungan and S. Lin, *Phys. Lett. A*, 2018, **38**, 2781–2786.
59 M. Naguib, M. Kurtoglu, V. Presser, J. Lu, J. Niu, M. Heon, L. Hultman, Y. Gogotsi and M. W. Barsoum, *Adv. Mater.*, 2011, **23**, 4248–4253.

60 M. Naguib, V. N. Mochalin, M. W. Barsoum and Y. Gogotsi, *Adv. Mater.*, 2014, **26**, 992–1005.
61 M. Naguib, O. Mashtalir, J. Carle, V. Presser, J. Lu, L. Hultman, Y. Gogotsi and M. W. Barsoum, *ACS Nano*, 2012, **6**, 1322–1331.
62 S. Wang, J.-X. Li, Y.-L. Du and C. Cui, *Comput. Mater. Sci.*, 2014, **83**, 290–293.
63 Y. Le Page and P. Saxe, *Phys. Rev. B: Condens. Matter Mater. Phys.*, 2002, **65**, 104104.
64 J. Wang, S. Yip, S. R. Phillpot and D. Wolf, *Phys. Rev. Lett.*, 1993, **71**, 4182–4185.
65 Z. Wu, E. Zhao, H. Xiang, X. Hao, X. Liu and J. Meng, *Phys. Rev. B: Conders. Matter. Phys.*, 2007, **76**, 054115.
66 A. Savin, R. Nesper, S. Wengert and T. F. Fassler, *Angew. Chem., Int. Ed. Engl.*, 1997, **36**, 1808–1832.
67 S. Gong, C. Zhang, S. Wang and Q. Wang, *J. Phys. Chem. C*, 2017, **121**, 10258–10264.
68 V. Wang and W. T. Geng, *J. Phys. Chem. C*, 2017, **121**, 10224.
69 C. R. Cooper, C. Lee, C. A. Marianetti, X. Wei, J. Hone and J. W. Kysar, *Phys. Rev. B: Condens. Matter Mater. Phys.*, 2013, **87**, 035423.
70 B. Mortazavi, O. Rahaman, M. Makaremi, A. Dianat, G. Cuniberti and T. Rabczuk, *Phys. E*, 2017, **87**, 228–232.
71 Q. Peng, C. Liang, W. Ji and S. De, *Phys. Chem. Chem. Phys.*, 2013, **15**, 2003–2011.
72 K. H. Michel and B. Verberck, *Phys. Rev. B: Condens. Matter Mater. Phys.*, 2009, **80**, 224301.
73 B. Mortazzvi, A. Dianat, O. Rahaman, G. Guniberti and T. Rabczuk, *J. Power Sources*, 2016, **329**, 456–461.
74 Q. Meng, A. Hu, C. Zhi and J. Fan, *Phys. Chem. Chem. Phys.*, 2017, **19**, 29106–29113.
75 M. Mortazavi, C. Wang, J. Deng, V. B. Shenoy and N. V. Medhekar, *J. Power Sources*, 2014, **268**, 279–286.
76 D. Er, J. Li, M. Naguib, Y. Gogotsi and V. B. Shenoy, *ACS Appl. Mater. Interfaces*, 2014, **6**, 11173–11179.
77 T. Yu, S. Zhang, F. Li, Z. Zhao, L. Liu, H. Xu and G. Yang, *J. Mater. Chem. A*, 2017, **5**, 18698–18706.
78 X. Lv, F. Li, J. Gong, J. Gu, S. Lin and Z. Chen, *Phys. Chem. Chem. Phys.*, 2020, **22**, 8902–8912.
79 (*a*) T. Bo, P. F. Liu, J. Xu, J. R. Zhong, Y. B. Chen, O. Eriksson, F. W. Wang and B. T. Wang, *Phys. Chem. Chem. Phys.*, 2018, **20**, 22168–22178; (*b*) T. Bo, P. F. Liu, J. Xu, J. R. Zhong, F. W. Wang and B. T. Wang, *Phys. Chem. Chem. Phys.*, 2019, **21**, 5178–5188.
80 A. Sibari, A. Marjaoui, M. Lakhal, Z. Kerrami, A. Kara, M. Benaissa, A. Ennaoui, M. Hamedoun, A. Benyoussef and O. Mounkachi, *Sol. Energy Mater. Sol. Cells*, 2018, **180**, 253–257.
81 X. Lv, W. Wei, Q. Sun, L. Yu, B. Huang and Y. Dai, *ChemPhysChem*, 2017, **18**, 1627–1634.
82 Y. Yu, Z. Guo, Q. Peng, J. Zhou and Z. Sun, *J. Mater. Chem. A*, 2019, **7**, 12145–12153.
83 G. Kresse and J. Hafner, *Phys. Rev. B: Condens. Matter Mater. Phys.*, 1993, **47**, 558.
84 C. Zhu, X. Qu, M. Zhang, J. Wang, Q. Li, Y. Geng, Y. Ma and Z. Su, *J. Mater. Chem. A*, 2019, **7**, 13356–13363.
85 J. Vetter, P. Novák, M. R. Wagner, C. Veitb, K.-C. Möller, J. O. Besenhard, M. Winter, M. Wohlfahrt-Mehrens, C. Vogler and A. Hammmouche, *J. Power Sources*, 2005, **147**, 269–281.